High-resolution simulations of non-Boussinesq downslope gravity currents in the acceleration phase

Albert Dai and Yu-lin Huang

Citation: Physics of Fluids **28**, 026602 (2016); doi: 10.1063/1.4942239
View online: http://dx.doi.org/10.1063/1.4942239
View Table of Contents: http://scitation.aip.org/content/aip/journal/pof2/28/2?ver=pdfcov
Published by the AIP Publishing

PHYSICS OF FLUIDS **28**, 026602 (2016)

High-resolution simulations of non-Boussinesq downslope gravity currents in the acceleration phase

Albert Dai[a] and Yu-lin Huang
Department of Engineering Science and Ocean Engineering, National Taiwan University, Taipei, Taiwan

(Received 3 August 2015; accepted 2 February 2016; published online 23 February 2016)

Gravity currents generated from an instantaneous buoyancy source of density contrast in the density ratio range of $0.3 \leq \gamma \leq 0.998$ propagating downslope in the slope angle range of $0° \leq \theta < 90°$ have been investigated in the acceleration phase by means of high-resolution two-dimensional simulations of the incompressible variable-density Navier-Stokes equations. For all density contrasts considered in this study, front velocity history shows that, after the heavy fluid is released from rest, the gravity currents go through the acceleration phase, reaching a maximum front velocity $U_{f,max}$, followed by the deceleration phase. It is found that $U_{f,max}$ increases as the density contrast increases and such a relationship is, for the first time, quantitatively described by the improved thermal theory considering the non-Boussinesq effects. Energy budgets show that, as the density contrast increases, the heavy fluid retains more fraction of potential energy loss while the ambient fluid receives less fraction of potential energy loss in the process of energy transfer during the propagation of downslope gravity currents. Previously, it was reported that for the Boussinesq case, the downslope gravity currents have a maximum of $U_{f,max}$ at $\theta \approx 40°$. It is found, as is also confirmed by the energy budgets in this study, that the slope angle at which the downslope gravity currents have a maximum of $U_{f,max}$ may increase beyond 40° as the density contrast increases. © *2016 AIP Publishing LLC.* [http://dx.doi.org/10.1063/1.4942239]

I. INTRODUCTION

Gravity currents, also known as buoyancy or density currents, are density-driven flows predominantly in the horizontal direction. A number of factors that are likely to cause variations in the density of fluid include temperature differentials, dissolved materials, and suspended sediments. In the literature, lock-exchange experiment, in which gravity currents are produced from a finite volume of heavy fluid and propagate on a horizontal boundary, has long served as a paradigm configuration in the study of gravity currents.[1–9] To date, most experimental, theoretical, and computational studies have addressed the Boussinesq case, in which the density difference between the heavy and light fluids is sufficiently small such that the influence of the density difference on the dynamics of gravity currents can be regarded as only via the driving body force associated with the acceleration of gravity.

Although the Boussinesq case is representative of many geophysical flows, the non-Boussinesq case, in which the density difference is significantly larger, can be important in quite a few situations, including spillage of industrial gases in a mine or into the atmosphere, fires in a tunnel or a room, snow avalanches, and pyroclastic flows from volcanic eruptions. In contrast, the non-Boussinesq lock-exchange flows have received comparatively less attention.[10–13] One plausible reason is that it is difficult to realize a wide range of density contrasts with "standard" working fluids that can be handled easily in the laboratory, e.g., salt water. Even with very expensive material

[a]hdai@ntu.edu.tw

such as sodium iodide, the density ratio, $\gamma = \tilde{\rho}_2/\tilde{\rho}_1$, where $\tilde{\rho}_1$ and $\tilde{\rho}_2$ represent the densities of the heavy and light fluids, respectively, can only reach as low as 0.61.[12]

In order to investigate the non-Boussinesq lock-exchange problem with larger density contrasts in more detail, highly resolved numerical simulations offer new possibilities, as demonstrated by Refs. 14–17 using high-resolution two-dimensional Navier-Stokes simulations. As long as the flow structures remain two-dimensional, the essential features of the flows are accurately captured by the simulations documented in these reports. It has also been confirmed by other researchers[18–22] that the three-dimensional vortex interactions are not important as long as the gravity currents remain in the acceleration phase and constant front velocity phase. Therefore, high-resolution two-dimensional Navier-Stokes simulations, as employed in this study, serve as a prevalent means to investigate the gravity currents in the acceleration phase and in the constant front velocity phase.

Compared with lock-exchange problem, gravity currents either down[23–25] or up a slope[26–28] are much less considered but are also commonly encountered in geological environments and engineering applications.[29–31] In some of these environments, e.g., snow avalanches and pyroclastic flows, the downslope gravity currents are not confined by the top wall because the height of the flow domain is essentially infinite, while in others, e.g., tunnel fires, the downslope gravity currents may be confined by the top wall. It is found by Ref. 22 that the lock-height-to-channel-height depth ratio, i.e., $\phi = \tilde{h}_0\tilde{L}_{x_3}^{-1}$, where $\tilde{h}_0$ and $\tilde{L}_{x_3}$ are the lock height and channel height in Figure 1, respectively, has a dominant influence on the qualitative features of the downslope gravity currents. For non-Boussinesq, full-depth ($\phi = 1$) lock-exchange flows in sloping channels, Ref. 18 observed the existence of a quasi-steady phase with constant front velocity. For Boussinesq downslope gravity currents in deep ambient ($\phi \to 0$), instead of a quasi-steady phase, Ref. 23 showed that the produced gravity currents go through an acceleration phase, reaching a maximum front velocity $U_{f,max}$, followed by a deceleration phase and the classic thermal theory was developed therein to describe the acceleration and deceleration phases of the propagation. Of course in the laboratory, a deep ambient environment with infinite channel height is unlikely to be reached physically. In fact, Ref. 23 experimentally investigated the propagation of a finite volume of heavy fluid down a slope in a channel, where the depth ratios were 0.16 and 0.13 for their two working channels. Nevertheless, Ref. 22 showed that the partial-depth lock-exchange flows with depth ratio $\phi = 0.16$ are sufficient to represent the deep ambient situation ($\phi \to 0$).

Similar to the lock-exchange flows, most studies in downslope gravity currents in deep ambient have addressed the Boussinesq case. The Boussinesq version of the problem set forth in Ref. 23 has been revisited by Ref. 32 for the influence of lock length, $\tilde{l}_0$, on the acceleration phase and by Refs. 24 and 25 for the deceleration phase. In particular, Ref. 32 reported that the acceleration phase is extended and the gravity currents behave more like a "starting plume" when the lock length to

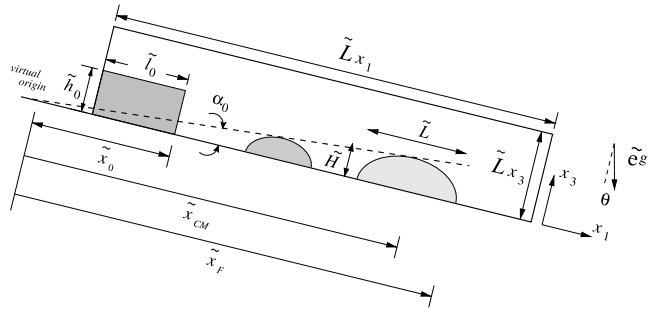

FIG. 1. Sketch for the gravity current propagating on a sloping boundary. Streamwise and wall-normal directions are denoted by x_1 and x_3, respectively. The domain of interest is set as $\tilde{L}_{x_1} \times \tilde{L}_{x_3}$, where $\tilde{L}_{x_1} = 10\tilde{l}_0$, $\tilde{L}_{x_3} = \tilde{h}_0\phi^{-1}$, and ϕ is the lock height to channel height ratio. In this study, $\tilde{l}_0 = 1.25\tilde{h}_0$ and $\phi = 0.16$ remain unchanged following previous experimental and computational studies.[22,23,25,37] Heavy fluid initially occupies the shaded region of $\tilde{h}_0 \times \tilde{l}_0$ without momentum. At $t = 0$, the heavy fluid is released and begins to propagate in the downslope direction, x_1. The gravity current head approximately takes the form of a semi-elliptical shape, with height $\tilde{H}$ and length $\tilde{L}$. The channel is inclined so the gravity vector $\tilde{e}^g$ makes an angle θ with the wall-normal direction, x_3.

lock height ratio, $l_0 = \tilde{l}_0/\tilde{h}_0$, increases. In the companion paper, Ref. 22 has investigated the Boussinesq downslope gravity currents in the acceleration phase using high-resolution two-dimensional Navier-Stokes simulations and it is found that a maximum of $U_{f,max}$ occurs at $\theta \approx 40°$. Here our focus is turned to the non-Boussinesq version of the problem set forth in Ref. 23. With the help of high-resolution two-dimensional Navier-Stokes simulations, the ranges of slope angle and density contrast investigated can be significantly increased and their influences on the dynamics of gravity currents in the acceleration phase can be seen more clearly.

The buoyancy source considered in this study is of finite volume of heavy fluid and the gravity currents are laterally confined as in a two-dimensional configuration. Other related studies include Ref. 33, who investigated the gravity currents produced from a finite volume of heavy fluid propagating on a laterally unconfined slope, and Refs. 34–36, who considered a buoyancy source of constant influx of heavy fluid into homogeneous and stratified environments.

The present study is a continuation of the computational investigation of the Boussinesq downslope gravity currents reported in the companion paper by Ref. 22 and also an extension of the experimental investigation of non-Boussinesq gravity currents by Ref. 37 in that gravity currents generated from an instantaneous, finite buoyancy source on different slopes were reported, where the density ratio was in the range of $0.85 \le \gamma \le 0.95$ and the slope was in the range of $0° \le \theta \le 9°$. As in many previous laboratory studies, the range of density contrast is limited by the solubility of sodium chloride in water at room temperature and the range of slope angle is limited by the flume height. Here the objective is to extend the study reported in Ref. 37 and investigate the influence of density contrast in a broader range of density ratio, i.e., $0.3 \le \gamma \le 0.998$, and in a broader range of slope angle, i.e., $0° \le \theta < 90°$. The lock length in this study follows[22,23,37] and remains unchanged as $l_0 = 1.25$. Since the influence of the depth ratio $\phi = \tilde{h}_0 \tilde{L}_{x_3}^{-1}$ has been reported in the companion paper by Ref. 22 and it has been confirmed that $\phi = 0.16$ is sufficient to represent gravity currents in deep ambient situation, in the simulations the depth ratio $\phi = 0.16$ is chosen following previous experimental and computational investigations of the downslope gravity currents in deep ambient case. In addition, since the influence of the Reynolds number has also been investigated in Ref. 22 and it has been reported that the influence of the Reynolds number is weak for $Re \gtrsim 4000$, we will not reinvestigate the influence of the Reynolds number and $Re = 4000$ is chosen in the simulations throughout. Our focus is on the acceleration phase of the propagation of gravity currents; therefore the investigation is conducted, as in the companion paper, by means of high-resolution two-dimensional simulations of the incompressible, variable-density Navier-Stokes equations.

II. IMPROVED THERMAL THEORY

Figure 1 shows the flow domain in this study and a schematic diagram of the gravity currents in the theory, where gravity currents are approximated by a semi-elliptical shape with aspect ratio $k = \tilde{H}/\tilde{L}$ during the propagation and $\tilde{H}$ and $\tilde{L}$ are the height and length of the semi-elliptical head, respectively. It is worth noting that the classic thermal theory was originally developed for the Boussinesq downslope gravity currents in deep ambient, i.e., $\gamma \approx 1$ and $\phi \to 0$, and has been used for many subsequent studies.[38,39] Here we further extend the classic thermal theory to include the non-Boussinesq effects, using the principles of momentum conservation, i.e.,

$$\frac{d\left(\tilde{\rho} + \tilde{\rho}_2 k_v\right) S_1 \tilde{H} \tilde{L} \tilde{U}}{d\tilde{t}} = \tilde{B} \sin\theta, \tag{1}$$

and mass conservation, i.e.,

$$\frac{d}{d\tilde{t}}(S_1 \tilde{H} \tilde{L}) = S_2 (\tilde{H} \tilde{L})^{1/2} \alpha(\theta) \tilde{U}. \tag{2}$$

Here the density of ambient fluid is taken as $\tilde{\rho}_2$ and the density of heavy fluid in the lock region is $\tilde{\rho}_1$. Initially the heavy fluid occupies the shaded region of which the area is $\tilde{A}_0 = \tilde{h}_0 \tilde{l}_0$. For non-Boussinesq gravity currents, $\tilde{\rho}_1$ typically serves as the reference density and a commonly used parameter characterizing the density difference is the density ratio, $\gamma = \tilde{\rho}_2/\tilde{\rho}_1$. The total buoyancy is defined to be $\tilde{B} = \tilde{g}(\tilde{\rho} - \tilde{\rho}_2) S_1 \tilde{H} \tilde{L}$. The cross-sectional area and the circumference

of the semi-elliptical head are defined as $S_1\tilde{H}\tilde{L}$ and $S_2(\tilde{H}\tilde{L})^{1/2}$, respectively, where $S_1 = \pi/4$ and $S_2 = (\pi/2^{3/2})(4k^2+1)^{1/2}/k^{1/2}$ are the shape factors. In addition, $\tilde{U}$ is the velocity of the centre of mass of the head, $k_v = 2k$ is the added mass coefficient,[40] and α is the entrainment coefficient.[41] Equation (2) yields self-similar solutions for $\tilde{H}$ and $\tilde{L}$ that grow linearly with distance, and the "virtual origin" is obtained by extrapolating $\tilde{H}$ upstream to $\tilde{H} = 0$.

Finally, when the heavy fluid is released from rest, the centre of mass velocity is given by

$$\tilde{U} = \left[C\left(\frac{2\gamma^2\left(X_B^3-1\right)-12\gamma\left(1-\gamma\right)Q\left(X_B-1\right)}{3\left(\gamma X_B^2+2\left(1-\gamma\right)Q\right)^2}\right)\right]^{1/2}, \tag{3}$$

where

$$C = 2\frac{1-\gamma}{\gamma}Q\tilde{g}\tilde{x}_0\sin\theta \quad \text{and} \quad Q = \frac{2k\tilde{A}_0}{(1+2k)\pi\alpha_0^2\tilde{x}_0^2} \tag{4}$$

are functions of density ratio γ, the distance from the virtual origin to the gate of release $\tilde{x}_0$, the angle of growth α_0, and $X_B = \tilde{x}_{CM}/\tilde{x}_0$. The front location, when measured from the virtual origin, is related to the position of the centre of mass by $\tilde{x}_F = (1+\alpha_0/2k)\tilde{x}_{CM}$ and likewise the front velocity is related to the centre of mass velocity by $\tilde{U}_f = (1+\alpha_0/2k)\tilde{U}$. When normalized by the velocity scale, $\sqrt{(1-\gamma)\tilde{g}\tilde{h}_0}$, the maximum dimensionless front velocity, $U_{f,max}$, has a closed-form solution and is novelly derived here as

$$U_{f,max} = \left(1+\frac{\alpha_0}{2k}\right)\left[\frac{2Q\tilde{x}_0\sin\theta}{\tilde{h}_0}\left(\frac{2\gamma\left(X_M^3-1\right)-12\left(1-\gamma\right)Q\left(X_M-1\right)}{3\left(\gamma X_M^2+2\left(1-\gamma\right)Q\right)^2}\right)\right]^{1/2}, \tag{5}$$

where

$$X_M = \Delta + \frac{1}{2}\sqrt{-4\Delta^2 - 24Q\frac{1-\gamma}{\gamma} + \frac{1}{\Delta}\left(4+24Q\frac{1-\gamma}{\gamma}\right)}, \tag{6}$$

with

$$\Delta = \frac{1}{2}\sqrt{\frac{1}{3}\left[13\,824Q^3\left(\frac{1-\gamma}{\gamma}\right)^3 + 27\left(4+24Q\frac{1-\gamma}{\gamma}\right)^2\right]^{\frac{1}{3}} - 8Q\frac{1-\gamma}{\gamma}}, \tag{7}$$

which reduces to $X_M = 4^{1/3}$ in the Boussinesq case and

$$U_{f,max} \approx 0.79\left(1+\frac{\alpha_0}{2k}\right)\left(\frac{Q\tilde{x}_0\sin\theta}{\tilde{h}_0}\right)^{1/2}, \tag{8}$$

as consistent with previously derived formula when $\gamma \to 1$.[22] An early version of the theory for non-Boussinesq downslope gravity currents, slightly different from that presented here due to the chosen scaling for the reference density, was formerly given in Ref. 42. In this study, we have improved the early version of the non-Boussinesq thermal theory by finding the closed-form solution, for the first time, for maximum front velocity (5). It will be shown in Sec. IV B that novelly derived formula (5) reasonably describes the relationship between the maximum front velocity and the density ratio. It is worth noting that the theoretical framework, which builds on parameters including the entrainment of ambient fluid, the angle of growth of the head, the semi-elliptical shape of the head, and, consequently, the shape factors, may not be readily applicable to the extreme case, $\gamma \ll 1$, such as water and air, because mixing between the two fluids in this situation is very limited. Nevertheless, the classic thermal theory offers a platform for improvement on which the non-Boussinesq effects can be considered, at least for the case when the density contrast is not extremely large.

III. NUMERICAL FORMULATION

Figure 1 also gives a sketch of the configuration for simulations of gravity currents down slopes. The heavy fluid of density $\tilde{\rho}_1$ is confined in the lock region and separated from the light fluid of density $\tilde{\rho}_2$. In most gravity current studies, the Boussinesq approximation, i.e., the density difference is sufficiently small such that the influence of density variations is retained only in the buoyancy term, has been employed. However, our intention is to consider cases in which the density contrast is larger, so the Boussinesq approximation will not be invoked. In the literature, there are a few computational studies of non-Boussinesq gravity currents[14,16,18] and in their formulation either the dynamic or the kinematic viscosity is assumed constant. In the following, we will keep the dynamic viscosity $\tilde{\mu}$ constant and the same for both fluids instead of a constant kinematic viscosity.[16] In fact, these two situations are equivalent for the Boussinesq case or when the Reynolds number is sufficiently high. Furthermore, it has been reported that these two situations are qualitatively consistent even when the density difference is larger.[14] Therefore, for incompressible, variable density flows, the dimensionless Navier-Stokes equations read

$$\frac{\partial u_k}{\partial x_k} = 0, \tag{9}$$

$$\rho\left(\frac{\partial u_i}{\partial t} + \frac{\partial u_i u_k}{\partial x_k}\right) = \frac{\rho}{1-\gamma} e_i^g - \frac{\partial p}{\partial x_i} + \frac{1}{Re}\frac{\partial^2 u_i}{\partial x_k \partial x_k}, \tag{10}$$

$$\frac{\partial \rho}{\partial t} + \frac{\partial \rho u_k}{\partial x_k} = \frac{1}{Pe}\frac{\partial^2 \rho}{\partial x_k \partial x_k}. \tag{11}$$

Here u_i denotes the velocity, ρ the density, γ the density ratio, e_i^g the unit vector in the direction of gravity, and p the pressure. The set of Equations (9)-(11) is made dimensionless by the lock height, $\tilde{h}_0$, as the length scale, the density of heavy fluid, $\tilde{\rho}_1$, as the reference density, the buoyancy velocity

$$\tilde{u}_b = \sqrt{\tilde{g}'\tilde{h}_0} \quad \text{with} \quad \tilde{g}' = (1-\gamma)\tilde{g}, \tag{12}$$

as the velocity scale, and $\tilde{h}_0\tilde{u}_b^{-1}$ as the time scale, where $\gamma = \tilde{\rho}_2/\tilde{\rho}_1$. Here the dimensionless density is defined as

$$\rho = \frac{\tilde{\rho}}{\tilde{\rho}_1}, \tag{13}$$

where $\gamma \le \rho \le 1$. By assuming a density-concentration relationship of the form $\tilde{\rho} = \tilde{\rho}_2 + c(\tilde{\rho}_1 - \tilde{\rho}_2)$, the concentration of fluid mixture c, where $0 \le c \le 1$, can be expressed in terms of the dimensionless density, ρ, as

$$c = \frac{\rho - \gamma}{1-\gamma}. \tag{14}$$

The Reynolds number Re and the Péclet number Pe arising in the dimensionless equations are defined by

$$Re = \frac{\tilde{u}_b\tilde{h}_0}{\tilde{\nu}} \quad \text{and} \quad Pe = \frac{\tilde{u}_b\tilde{h}_0}{\tilde{\kappa}}, \tag{15}$$

respectively, where $\tilde{\nu}$ is the kinematic viscosity of the heavy fluid and $\tilde{\kappa}$ is the diffusion coefficient for both the heavy and light fluids. The Reynolds number and the Péclet number are related by the Schmidt number

$$Sc = \frac{\tilde{\nu}}{\tilde{\kappa}}, \tag{16}$$

which represents the ratio of the kinematic viscosity to molecular diffusivity. It has been observed by many researchers[43–46] that the influence of Schmidt number on the dynamics of the gravity current is weak as long as $Sc \approx O(1)$ or larger, so we employ $Sc = 1$ throughout. But it should still be kept in mind that typically in saline experiments, $Sc \approx 700$.

The set of equations in the velocity-pressure formulation is solved in the flow domain with resolution $N_{x_1} \times N_{x_3}$. The channel running length in the streamwise direction, L_{x_1}, was chosen ten times larger than the length of the lock to allow full development of the acceleration phase. The influence of the depth ratio, $\phi = \tilde{h}_0 \tilde{L}_{x_3}^{-1}$, has been reported in the companion paper and has been confirmed to be negligible for sufficiently low values of ϕ. Here we set $\phi = 0.16$ in the simulations throughout. Fourier expansion with the periodic boundary condition is employed in the streamwise direction. To ensure a reflection condition at the left wall ($x_1 = 0$) as in the experiments and to prevent any upslope propagation upon the release of heavy fluid, an image is placed to the left of the domain of interest such that the heavy fluid in the lock is fully discharged into the channel of length L_{x_1}.[21,22] Chebyshev expansion with Gauss-Lobatto quadrature points is employed in the wall-normal direction. The Gauss-Lobatto quadrature points provide a straightforward implementation of boundary conditions and have high resolution near the walls. Previous computational studies[14,20] have shown that the slip boundary conditions allow the gravity currents to propagate faster but do not change the dominant qualitative features of the flow; therefore the influence of the boundary conditions will not be reinvestigated in this study. Here we employ no-slip and no-flux conditions at the top and bottom walls for the velocity and density fields, respectively.

The flow field is advanced in time by the low-storage third-order Runge-Kutta scheme.[47] The inertia term on the left hand side of (10), i.e., $\rho Du_i/Dt$, can be separated into two parts, namely, $\gamma Du_i/Dt$ and $(\rho - \gamma)Du_i/Dt$, where the latter part is regarded as a non-Boussinesq forcing term. The convection, buoyancy, and non-Boussinesq forcing terms are treated explicitly while the diffusion terms are treated implicitly with Crank-Nicolson scheme. To reduce the aliasing error, Arakawa method[48] is used to evaluate the convection term alternately between divergence and convective forms. The Boussinesq version of the de-aliased pseudospectral code has been employed for lock-exchange flows[45,49] and for downslope gravity currents,[20–22] to which the readers are referred for more details of the implementation of the code. In all simulations, the velocity field was initialized with quiescent condition everywhere. The initial density field is prescribed unity in the heavy fluid region and zero elsewhere with a smooth error-function type transition in the interface region.[50] With increasing Re the complexity and required resolution increase. To resolve the full flow structures of the gravity currents in the domain $L_{x_1} \times L_{x_3} = 10 l_0 \times \phi^{-1}$, adequate resolution requires a grid size of $\Delta x_1 \approx (ReSc)^{-1/2}$ in the streamwise direction and a typical grid of $N_{x_1} \times N_{x_3} = 672 \times 420$ is used for $\phi = 0.16$, $l_0 = 1.25$, and $Re = 4000$. The time step was chosen to produce a Courant number less than 0.5.

IV. RESULTS

A. Representative Boussinesq case

For validation purposes, we first consider a representative case with a slope of 9° and a density ratio $\gamma = 0.998$, at which the Boussinesq approximation is valid. This representative Boussinesq case has also been investigated experimentally by Refs. 23 and 25 and computationally by Ref. 22. In this situation, the results obtained by solving the present variable-density equations should agree with our earlier results based on the Boussinesq equations.[22] Figure 2 shows the concentration and vorticity contours for $Re = 4000$. As time progresses, the heavy fluid collapses and the two roll-up vortices accomplish a complete overturn in the leapfrog process, as shown in Figure 2 at $t = 1.77$–7.95. Towards the end of the acceleration phase, a large roller is left behind the current front. This observation is consistent with the experimental observation previously made by Ref. 25 and also with the computational observation for the Boussinesq downslope gravity currents made by Ref. 22, because the present simulation at $\gamma = 0.998$ closely reproduces the Boussinesq simulation results, cf. Figure 2(f). For the Boussinesq gravity currents, it is reported by Ref. 22 that such a complete vortex overturn and a large roller structure are persistent for gravity currents on slope angles greater than 6°.

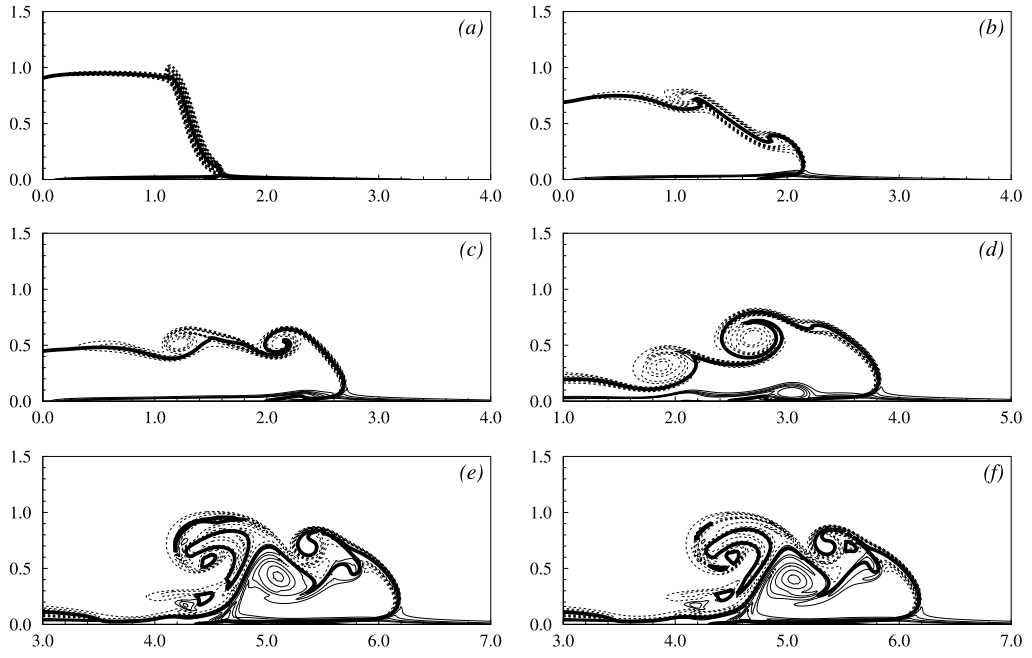

FIG. 2. A planar gravity current propagating on a 9° slope at $\gamma = 0.998$ and $Re = 4000$. Flow evolution is visualized by the concentration and vorticity contours at (a) $t = 0.88$, (b) 1.77, (c) 2.65, (d) 4.42, (e) 7.95. Here the thick solid lines represent $c = 0.5$ and thin solid (dashed) lines represent positive (negative) vorticity contours. (f) shows the concentration and vorticity contours from a corresponding Boussinesq simulation at $t = 7.95$. The non-Boussinesq simulation at $\gamma = 0.998$ and the Boussinesq simulation give very close results.

In order to measure the front location of gravity currents, we define the equivalent height $h(x_1,t)$ following previous works[1,14,18,45] as

$$h(x_1,t) = \frac{1}{1-\gamma}\int_0^{L_{x_3}} \rho(x_1,x_3,t)dx_3 - \frac{\gamma}{1-\gamma}. \tag{17}$$

Equivalent height is essentially a compact measure of the distribution of heavy fluid along the streamwise direction. Figure 3 shows the equivalent height evolution for the gravity currents on a 9° slope at two density ratios, i.e., $\gamma = 0.998, 0.4$. The front location, x_f, can be identified unambiguously as the furthest location reached by the gravity currents and the front velocity, U_f, can be derived using the front location data, via $U_f = dx_f/dt$. The qualitative influence of density ratio on the propagation of gravity currents is clear in Figure 3. For a given slope angle, the equivalent height of a gravity current decreases as the density ratio decreases. Such an observation indicates that as the density ratio decreases, the heavy fluid tends to spread in the streamwise direction more rapidly with less tendency to engage light ambient fluid in the propagation.

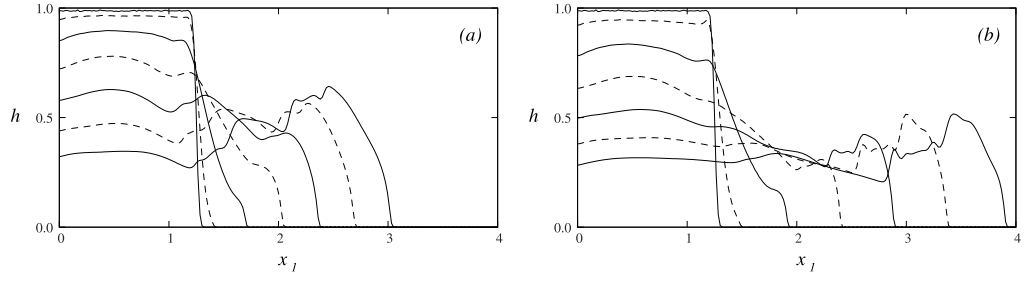

FIG. 3. Evolution of equivalent height of gravity currents on a 9° slope at $Re = 4000$ for two density ratios, i.e., $\gamma = 0.998$ (a) and $\gamma = 0.3$ (b). The time interval between consecutive equivalent height profiles is chosen at 0.53 dimensionless units.

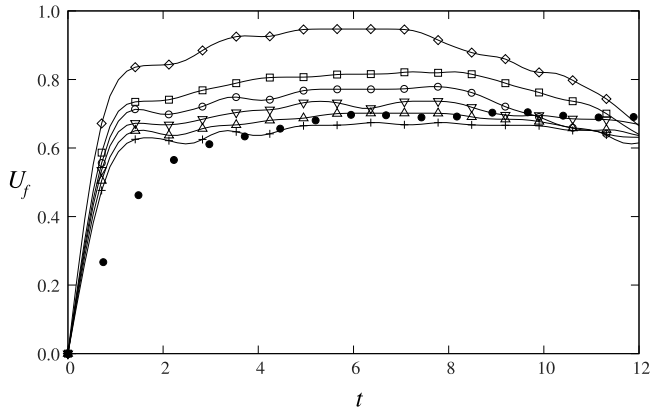

FIG. 4. Front velocity versus time for gravity currents propagating on a 9° slope at $Re = 4000$ for different density ratios. Symbols: +, $\gamma = 0.998$; △, $\gamma = 0.9$; ▽, $\gamma = 0.8$; ○, $\gamma = 0.7$; □, $\gamma = 0.6$; ◇, $\gamma = 0.4$; •, experiments from Ref. 25 in which $\gamma \approx 0.98$ and $Re \approx 9000$.

Figure 4 shows the front velocity versus time for gravity currents on a 9° slope with different density ratios, including the Boussinesq case ($\gamma \approx 1$). After the heavy fluid is released, the front velocity of the Boussinesq downslope gravity currents rapidly increases from zero with maximum acceleration until $t \approx 1.2$. In the latter part of the acceleration phase, the front velocity continues to increase but with a reduced acceleration until a maximum front velocity is reached. The observation is consistent with recent experiments reported by Ref. 25, as also shown in Figure 4.

B. Influence of the density contrast

As a next step, we consider $\gamma = 0.9$, again for $\theta = 9°$ and $Re = 4000$. This density ratio is close to the limit where the Boussinesq approximation loses its validity. Figure 5(a) demonstrates that the vortex overturn is completed at $t = 7.95$ and the differences between the results of the cases $\gamma = 0.998$ and $\gamma = 0.9$ are relatively small. As the density contrast further increases, i.e., $\gamma = 0.8, 0.7, 0.6$, a qualitatively new feature emerges. While the vortices along the frontal region of the current head remain strong, the complete vortex overturn in the Boussinesq case now ceases to exist. Instead, one of the two roll-up vortices remains in the tail current, as seen between $3 < x_1 < 4$ in Figures 5(b)–5(d). The observation is also consistent with recent experiments that the roller forming behind the head is smaller than the Boussinesq counterpart, as reported in Ref. 37 and shown in Figure 6.

More different features emerge in the non-Boussinesq downslope gravity currents. As shown in Figures 4 and 5, the non-Boussinesq downslope gravity currents propagate at higher speeds as the density contrast increases, which is in good agreement with the experimental observations of Ref. 37. By the notion of mass conservation and as also observed in Figure 3, the equivalent height of the gravity currents should decrease as the density contrast increases. The angle of growth, α_0, decreases while the distance from the virtual origin to the gate, x_0, increases with increasing density contrast, as shown in Figure 7(a).

With the help of the improved thermal theory considering the non-Boussinesq effects and the empirical relationships for x_0 and α_0 in Figure 7(a), the relationship between the maximum front velocity and the density ratio can be reasonably described by novelly derived formula (5), as demonstrated by the dashed line in Figure 7(b). Here the maximum front velocity derived from the simulation results is in good agreement with the experimental results, even though the Reynolds number in the experiments, ranging from $Re \approx 9000$ for $\gamma = 0.998$ to $Re \approx 26\,000$ for $\gamma = 0.85$, is higher than the Reynolds number in the simulations. As demonstrated by Ref. 22, the influence of the Reynolds number on the maximum front velocity is weak for $Re \gtrsim 4000$ and here a good agreement between the simulation and experimental results is expected for sufficiently high Reynolds numbers. Interestingly, as the density contrast increases, the maximum front velocity of downslope gravity

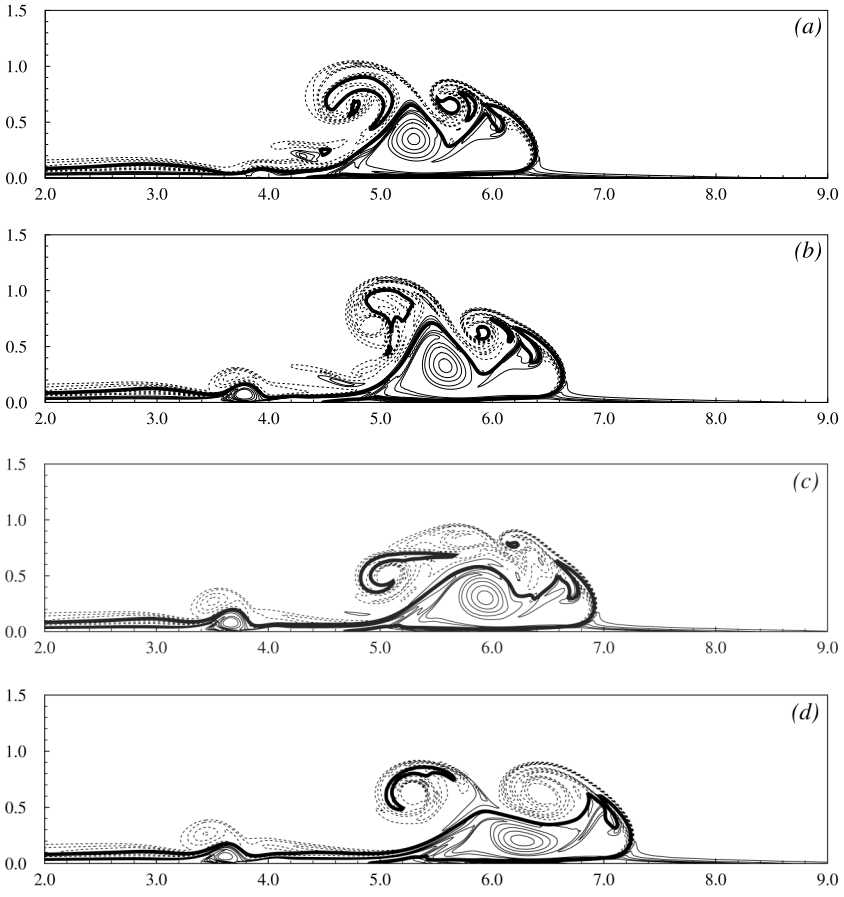

FIG. 5. Flow patterns of gravity currents on a 9° slope with four different density ratios from simulations. Panels: (a) $\gamma = 0.9$, (b) 0.8, (c) 0.7, (d) 0.6. Flow patterns are visualized by the concentration and vorticity contours. Here the thick solid lines represent $c = 0.5$ and thin solid (dashed) lines represent positive (negative) vorticity contours. Reynolds number is chosen at $Re = 4000$ in the simulations and time instance is chosen at $t = 7.95$ dimensionless units.

currents $U_{f,max}$ is related to that of the Boussinesq case $U_{f,max(\gamma\approx1)}$ by $U_{f,max} \approx U_{f,max(\gamma\approx1)}\gamma^{-1/2}$, as demonstrated by the dashed line in Figure 7(b). Although this relationship $U_{f,max} \sim \gamma^{-1/2}$ cannot be derived merely based on theoretical arguments, it appears to be a reasonable approximation for the range of density ratio considered in this study. For brevity, only results of gravity currents on a 9° slope are presented here as the results on other slope angles are qualitatively similar.

C. Mixing

It has been reported in the companion paper and also in previous studies[18,22,41,51] that the large-scale vortex overturn events and the mixing of fluids, characterized by the area of the mixed

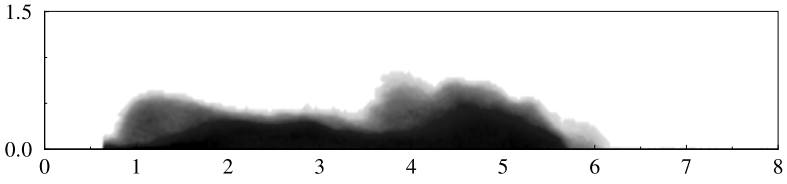

FIG. 6. Image from the experiment 01/29/13 – 5 reported by Ref. 37 for the gravity current from a buoyancy source of $\tilde{l}_0/\tilde{h}_0 = 10\text{cm}/8\text{cm}$ and density ratio $\gamma \approx 0.85$ propagating on a 9° slope. Distances in the downslope and wall-normal directions are normalized by the lock height, $\tilde{h}_0$. Time instance is chosen at $t \approx 8$ dimensionless units. Reynolds number in the experiment is at $Re \approx 26\,000$.

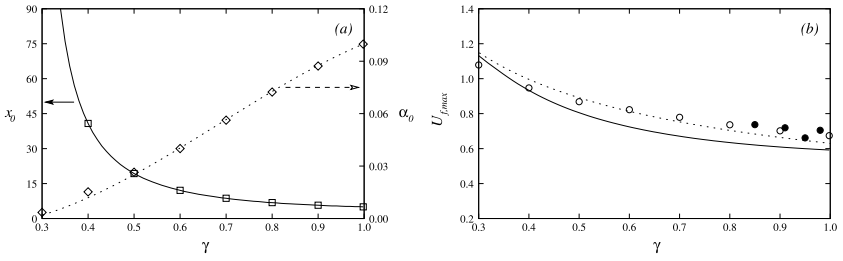

FIG. 7. Influence of the density ratio, γ, on the parameters of gravity currents on a 9° slope at $Re = 4000$. Panel (a) shows the angle of growth α_0, designated by ◇, and the distance from the virtual origin to the gate x_0, designated by □, against the density ratio γ, where solid and dashed lines represent the interpolating functions for x_0, i.e., $x_0 \approx 3.66\gamma^{2.74}$, and for α_0, i.e., $\alpha_0 \approx -1.84\times10^{-1}\gamma^3 + 3.80\times10^{-1}\gamma^2 - 9.78\times10^{-2}\gamma + 2.00\times10^{-3}$, respectively. Panel (b) shows the maximum front velocity $U_{f,max}$ against the density ratio γ, where ○ represents the computational data in this study, ● represents the experimental data,[37] in which the Reynolds number in the experiments ranges from $Re \approx 9000$ for $\gamma = 0.998$ to $Re \approx 26\,000$ for $\gamma = 0.85$, solid line represents the theoretical prediction based on (5) and dashed line represents the approximation $U_{f,max} \sim \gamma^{-1/2}$.

region where the concentration is in the range of $0.1 \le c \le 0.9$, are influenced by the slope angle. In the Boussinesq case, the area of the mixed region at a given instant in time increases uniformly with increasing slope angle. It is worth noting that here in the acceleration phase, these large-scale vortex structures are predominantly two-dimensional but are subject to three-dimensional breakdown in the deceleration phase.[19,21,45]

In order to illustrate the dependence of the mixing on the density ratio, we again restrict our attention to the gravity currents on a 9° slope at $Re = 4000$. In order to quantify the mixing,[18,22] we define the mixed region where the density is within the range of

$$\tilde{\rho}_2 + \frac{1}{10}\Delta\tilde{\rho} < \tilde{\rho} < \tilde{\rho}_1 - \frac{1}{10}\Delta\tilde{\rho}, \tag{18}$$

where $\Delta\tilde{\rho} = \tilde{\rho}_1 - \tilde{\rho}_2$. Figure 8 shows the size of mixed region versus front location and versus time for different density ratios, where the size of mixed region is non-dimensionalized by the square

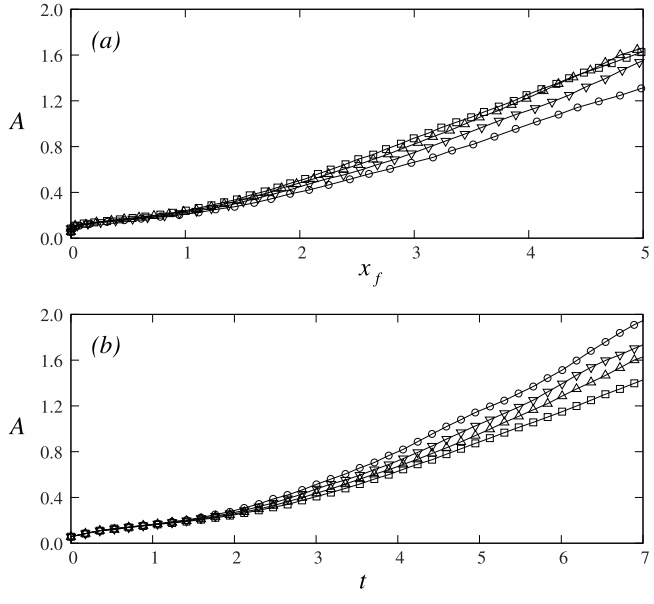

FIG. 8. The size of the mixed region versus front location x_f is plotted in panel (a) and the size of mixed region versus time is plotted in panel (b) for gravity currents on a 9° slope at $Re = 4000$ for different density ratios. Symbols: □, $\gamma = 0.9$; △, $\gamma = 0.7$; ▽, $\gamma = 0.5$; ○, $\gamma = 0.3$.

of the length scale, i.e., $\tilde{h}_0^2$. For gravity currents on a 9° slope at $Re = 4000$, the acceleration phase spans spatially in the range of $0 \le x_f \lesssim 5$ and temporally in the range of $0 \le t \lesssim 7$. It is observed that in the initial part of the acceleration phase, i.e., $0 \le x_f \lesssim 1.1$ and $0 \le t \lesssim 1.4$, mixing is not sensitively influenced by the density ratio, while in the latter part of the acceleration phase, the influence of the density ratio is apparent. As intuitively expected and as shown in Figure 8(a), when the size of mixed region is plotted against the front location, the size of mixed region at a given front location decreases uniformly as the density ratio decreases. This observation is consistent with the observation in the equivalent height, as shown in Figure 3, and also with the notion that the overturn events are less likely to occur when the density ratio decreases, as shown in Figure 5. When the size of mixed region is plotted against time, as shown in Figure 8(b), the size of mixed region at a given instant in time increases uniformly as the density ratio decreases. The observations on the size of mixed region versus front location and versus time reflect the fact that the front velocity increases with increasing density contrast, as illustrated in Figures 4 and 7.

D. Energy budgets

From the point of view of energy budgets, the propagation of gravity currents on an inclined boundary is essentially a conversion process of the available potential energy into kinetic energy and subsequently into dissipation by viscous friction. As demonstrated for the Boussinesq case in the companion paper by Ref. 22, the potential energy loss is more efficiently converted into the kinetic energy associated with ambient fluid, with less fraction of energy being converted into the kinetic energy associated with heavy fluid and being dissipated as the slope angle increases. In order to illustrate the dependence of the above picture of energy budgets on the density contrast, we again restrict our attention to the gravity currents on a 9° slope with different density ratios. In the following we will provide a computational analysis of the overall energy budget.

The equation for the time derivative of the kinetic energy is obtained by multiplying the momentum equation (10) by u_i, i.e.,

$$\frac{D}{Dt}\left(\frac{1}{2}\rho u_i u_i\right) = -\frac{\partial}{\partial x_i}(p u_i) + \frac{2}{Re}\frac{\partial}{\partial x_j}(s_{ij}u_i) - \frac{2}{Re}s_{ij}s_{ij} + \frac{\rho}{1-\gamma}(\sin\theta u - \cos\theta w), \tag{19}$$

where D/Dt denotes the material derivative and $s_{ij} = \frac{1}{2}(u_{i,j} + u_{j,i})$ denotes the strain rate tensor. Integration of (19) over the entire flow domain Ω leads to the evolution equation of the total kinetic energy K, i.e.,

$$\frac{dK}{dt} = -\frac{2}{Re}\int_\Omega s_{ij}s_{ij}dV + \int_\Omega \frac{\rho}{1-\gamma}(\sin\theta u - \cos\theta w)\,dV, \quad K(t) = \int_\Omega \frac{1}{2}\rho u_i u_i dV, \tag{20}$$

where the divergence terms on the right-hand side of (19) vanish after integration. The kinetic energy K can be decomposed into two parts, i.e.,

$$K(t) = \int_\Omega \frac{1}{2}c u_i u_i dV + \gamma\int_\Omega \frac{1}{2}(1-c)u_i u_i dV, \tag{21}$$

where the first part on the right hand side of (21), designated by K_H, is associated with heavy fluid and the second part, designated by K_L, is associated with ambient fluid. The effects of diffusion in the density field on the potential energy can be neglected for gravity currents in the acceleration phase,[14,22,52] and the potential energy in the system is

$$E_p(t) = \int_\Omega \frac{\rho}{1-\gamma}[x_3\cos\theta + (L_{x_1} - x_1)\sin\theta]dV, \tag{22}$$

and the second term on the right-hand side of (20) represents the additive inverse of the time derivative of the potential energy in the system. The potential energy in the system can similarly be decomposed into two parts, i.e.,

$$E_p(t) = \frac{\gamma}{1-\gamma}\int_\Omega [x_3\cos\theta + (L_{x_1} - x_1)\sin\theta]dV + \int_\Omega c[x_3\cos\theta + (L_{x_1} - x_1)\sin\theta]dV, \tag{23}$$

where the first part on the right hand side of (23) is the potential energy associated with ambient fluid, which is invariant during the propagation of gravity currents, and the second part is the available potential energy, E_p^e, only which can be converted into kinetic energy and be dissipated consequently. The first term on the right-hand side of (20) represents the dissipation and we use E_d to denote the time integral of dissipation, i.e.,

$$E_d(t) = \int_0^t \epsilon(\tau) d\tau, \quad \epsilon = \frac{2}{Re} \int_\Omega s_{ij} s_{ij} dV. \tag{24}$$

In other words, Equation (20) is essentially a statement of conservation of energy, i.e., that $K + E_p^e + E_d$ is a constant during the propagation of gravity currents. Since our focus is on the acceleration phase of the propagation, we use the available potential energy drop in the acceleration phase, ΔE_p^e, to normalize all contributions to the energy budget. Here the superscript n denotes normalized contributions.

Figure 9 shows the time histories of the normalized kinetic energy and dissipated energy during the propagation of gravity currents on a 9° slope with $\phi = 0.16$, $l_0 = 1.25$, and $Re = 4000$ at three different density ratios, i.e., $\gamma = 0.998$, 0.7, and 0.4. The overall energy is conserved with high accuracy in the acceleration phase and the maximum error is within 1%. It is observed that, as the density contrast increases, less fraction of potential energy loss is converted into the total kinetic energy, $(K_H^n + K_L^n)$, and more fraction of potential energy loss is dissipated. Interestingly, qualitatively distinct dependences of the kinetic energy associated with heavy fluid, K_H^n, and that associated with ambient fluid, K_L^n, on the density contrast are observed for the first time. As clearly shown in Figure 9, the time at which K_L^n supersedes K_H^n increases as the density contrast increases. As the density contrast increases, the heavy fluid retains more fraction of potential energy loss and K_H^n increases for a longer period of time, while the ambient fluid receives less fraction of potential energy loss. Here a physical argument may help explain this observation. As the density contrast increases, the interface between the heavy and light ambient fluids becomes more stable against roll-up and overturns, through which the ambient fluid is engaged in the convection and heavy fluid imparts energy upon the ambient fluid. Therefore, the potential energy loss is less prone to being converted into the kinetic energy associated with ambient fluid with increasing density contrast.

E. Influence of the slope angle

The influence of the slope angle on the Boussinesq downslope gravity currents has been investigated by Ref. 22. It is reported that a maximum front velocity for the Boussinesq downslope gravity currents exists near $\theta = 40°$, above which the ambient fluid retains more kinetic energy than the heavy fluid during the propagation of gravity currents right from the outset. In this section, we investigate how the influence of the slope angle in the Boussinesq case is modified when the density contrast increases.

Figure 10 shows the front velocity histories and energy budgets for gravity currents with $\phi = 0.16$, $l_0 = 1.25$, and $Re = 4000$ at two slope angles, i.e., $\theta = 9°, 70°$, and at two density ratios, i.e., $\gamma = 0.998, 0.7$. Here the slope angles and density ratios are chosen for illustrative purposes. The overall energy is conserved with high accuracy and again the maximum error is within 1%.

Interesting features of the energy budgets are observed. In the left column of Figure 10, namely, for the gravity currents on a 9° slope, the kinetic energy associated with heavy fluid, K_H^n, initially grows faster than that associated with ambient fluid, K_L^n, before K_L^n overtakes K_H^n towards the end of the acceleration phase. In the right column of Figure 10 for gravity currents on a 70° slope, the kinetic energy associated with ambient fluid, K_L^n, increases as the slope angle increases while the kinetic energy associated with heavy fluid, K_H^n, and the normalized dissipated energy, E_d^n, decrease as the slope angle increases.

For the Boussinesq case ($\gamma \approx 1$), it is known that the potential energy loss is equally converted into the kinetic energy associated with heavy fluid and that associated with ambient fluid for the most part of the acceleration phase at $\theta \approx 40°$, at which $U_{f,max}$ reaches its maximum value. When the density contrast increases, as illustrated in Figure 10, the potential energy loss is less prone to being converted into the kinetic energy associated with ambient fluid. For larger density contrasts,

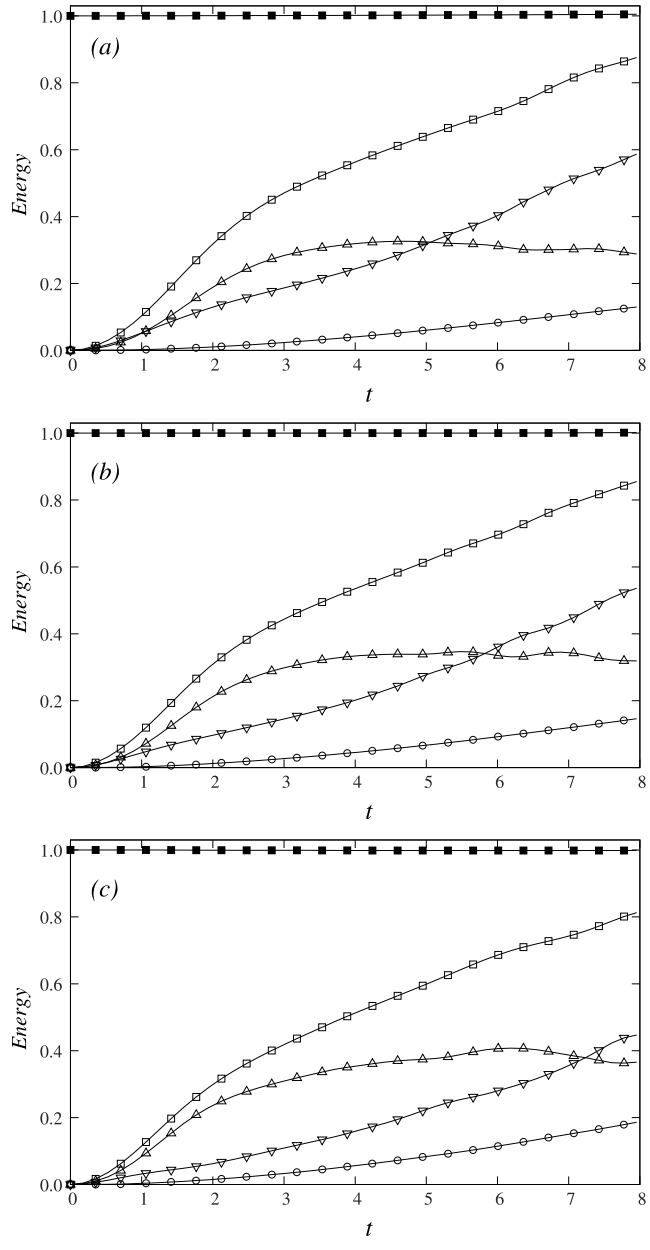

FIG. 9. The normalized total energy, kinetic energy, dissipated energy as functions of time for gravity currents on a 9° slope at $Re = 4000$. All contributions to the energy budget are normalized by the potential energy loss from $t = 0$ to $t = 8$. Three different density ratios, i.e., $\gamma = 0.998, 0.7, 0.4$, are chosen for illustrative purposes. Panels: (a) $\gamma = 0.9988$, (b) 0.7, (c) 0.4. Symbols: ■, total energy; □, kinetic energy K^n; △, kinetic energy associated with heavy fluid K_H^n; ▽, kinetic energy associated with ambient fluid K_L^n; ○, dissipated energy E_d^n.

therefore, the slope angle is anticipated to increase beyond 40° in order for the potential energy loss to be equally converted into K_H^n and K_L^n for the initial part of the acceleration phase.

The observations in the energy budgets imply that the slope angle at which the maximum front velocity $U_{f,max}$ occurs could increase as the density contrast increases. Such an implication is further confirmed by the maximum front velocity versus slope angle for different density ratios, as shown in Figure 11. Physically, such an observation reflects the fact that, as discussed previously, the ambient fluid is less likely to be engaged in the conversion process of potential energy loss into the kinetic energy associated with ambient fluid as the density contrast increases. In order for the ambient fluid to be more easily engaged in the energy transfer process, the slope angle must further

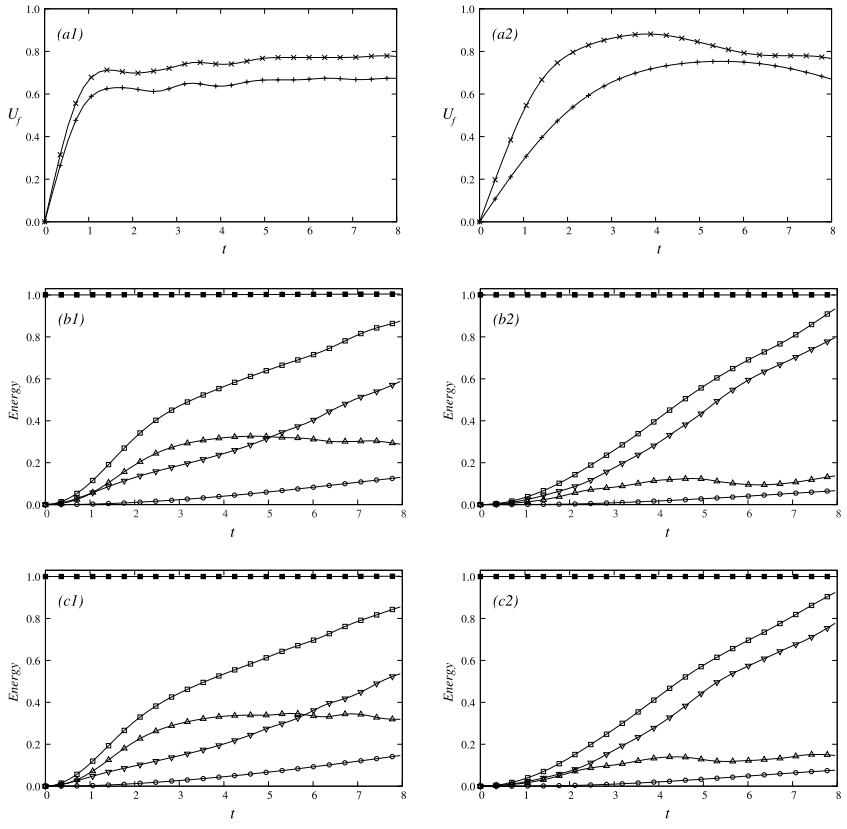

FIG. 10. Front velocity and the normalized total energy, kinetic energy, dissipated energy as functions of time for gravity currents at $Re = 4000$ for different slope angles and density ratios. All contributions to the energy budget are normalized by the potential energy loss from $t = 0$ to $t = 8$. Two slope angles, i.e., $\theta = 9°, 70°$, and two density ratios, i.e., $\gamma = 0.998, 0.7$, are chosen for illustrative purposes. Panels: (a1) front velocity for $\theta = 9°$, $\gamma = 0.998$ (represented by +), 0.7 (represented by ×); (a2) front velocity for $\theta = 70°$, $\gamma = 0.998$ (represented by +), 0.7 (represented by ×); (b1) energy budgets for $\theta = 9°$, $\gamma = 0.998$; (b2) energy budgets for $\theta = 70°$, $\gamma = 0.998$; (c1) energy budgets for $\theta = 9°$, $\gamma = 0.7$; (c2) energy budgets for $\theta = 70°$, $\gamma = 0.7$. Symbols: ■, total energy; □, kinetic energy K^n; △, kinetic energy associated with heavy fluid K_H^n; ▽, kinetic energy associated with ambient fluid K_L^n; ○, dissipated energy E_d^n.

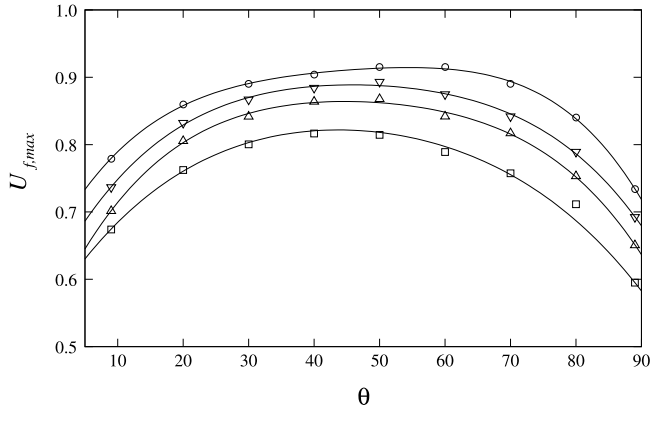

FIG. 11. The maximum front velocity $U_{f,max}$ against slope angle for gravity currents at $Re = 4000$ at four different density ratios. Symbols: □, $\gamma = 0.998$; △, $\gamma = 0.9$; ▽, $\gamma = 0.8$; ○, $\gamma = 0.7$.

increase to allow for more destabilizing effects, including a decreasing wall-normal component of gravity and an increasing downslope component of gravity, as explained by Refs. 22 and 53.

V. CONCLUSIONS

The paper presents high-resolution two-dimensional Navier-Stokes simulations of non-Boussinesq downslope gravity currents in the acceleration phase. In the laboratory, the range of slope angle and the range of density contrast are both limited by the accessible apparatus and working fluids. With the help of simulations, investigation of non-Boussinesq downslope gravity currents with density ratio in the range of $0.3 \leq \gamma \leq 0.998$ and slope angle in the range of $0^\circ \leq \theta < 90^\circ$ becomes feasible.

Our results show that for all density ratios considered in the study, two parts of the acceleration phase can be identified based on the front velocity history, namely, the initial part with maximum acceleration followed by the latter part where the acceleration is reduced, before reaching the maximum front velocity $U_{f,max}$. In the latter part of the acceleration phase, the interface between the heavy and light ambient fluids may roll up into a pair of vortices, which may further accomplish a complete overturn for slope angles greater than 6° in the Boussinesq case. As the density contrast increases, the roll-up vortices may not accomplish a complete overturn as in the Boussinesq case and the maximum front velocity $U_{f,max}$ increases.

In the Boussinesq case, it is found that a maximum of $U_{f,max}$ exists at $\theta \approx 40^\circ$, at which slope angle the potential energy loss is equally converted into the kinetic energy associated with heavy fluid and that associated with ambient fluid for the most part of the acceleration phase. As the density contrast increases, energy budgets show that the heavy fluid retains more fraction of potential energy loss while the ambient fluid receives less fraction of potential energy loss as the gravity currents propagate. As the density contrast increases, the interface between the heavy and light ambient fluids becomes more stable against roll-up and overturns and the ambient fluid is less ably to be engaged in the energy transfer process.

A special feature in the non-Boussinesq downslope gravity currents is that the slope angle, at which a maximum of $U_{f,max}$ occurs, may increase beyond 40° as the density contrast increases. Such an observation is also confirmed by the energy budgets. In order for the ambient fluid to be more easily engaged in the energy transfer process and for the maximum of $U_{f,max}$ to exist, the slope angle must further increase beyond 40° to facilitate the energy transfer of potential energy loss to the kinetic energy associated with ambient fluid.

ACKNOWLEDGMENTS

The author wishes to thank the encouragement from Professor Paul Linden and Professor Stuart Dalziel at the University of Cambridge, S. Balachandar at the University of Florida, Marcelo Garcia and Gary Parker at the University of Illinois at Urbana-Champaign, C. C. Hsu at Tamkang University, and Bill Peirson at the University of New South Wales. Computational resources are provided by National Taiwan University and Tamkang University. The research is supported by Taiwan Ministry of Science and Technology through Grant No. MOST-104-2628-E-002-012-MY3, National Taiwan University through Grant Nos. NTU-CDP-104R7815 and NTU-CDP-105R7815, and TSUNG Cho-chang Education Foundation through Grant No. 104-S-A10.

[1] J. Shin, S. Dalziel, and P. Linden, "Gravity currents produced by lock exchange," J. Fluid Mech. **521**, 1–34 (2004).
[2] B. Marino, L. Thomas, and P. Linden, "The front condition for gravity currents," J. Fluid Mech. **536**, 49–78 (2005).
[3] M. La Rocca, C. Adduce, G. Sciortino, and A. B. Pinzon, "Experimental and numerical simulation of three-dimensional gravity currents on smooth and rough bottom," Phys. Fluids **20**, 106603 (2008).
[4] M. La Rocca, C. Adduce, V. Lombardi, G. Sciortino, and R. Hinkermann, "Development of a lattice Boltzmann method for two-layered shallow-water flow," Int. J. Numer. Methods Fluids **70**, 1048–1072 (2012).
[5] M. La Rocca, C. Adduce, G. Sciortino, P. A. Bateman, and M. A. Boniforti, "A two-layer shallow water model for 3D gravity currents," J. Hydraul. Res. **50**, 208–217 (2012).
[6] C. Adduce, G. Sciortino, and S. Proietti, "Gravity currents produced by lock-exchanges: Experiments and simulations with a two layer shallow-water model with entrainment," J. Hydraul. Eng. **138**, 111–121 (2012).

[7] H. I. S. Nogueira, C. Adduce, E. Alves, and M. J. Franca, "Analysis of lock-exchange gravity currents over smooth and rough beds," J. Hydraul. Res. **51**, 417–431 (2013).
[8] H. I. S. Nogueira, C. Adduce, E. Alves, and M. J. Franca, "Image analysis technique applied to lock-exchange gravity currents," Meas. Sci. Technol. **24**, 047001 (2013).
[9] H. I. S. Nogueira, C. Adduce, E. Alves, and M. J. Franca, "Dynamics of the head of gravity currents," Environ. Fluid Mech. **14**, 519–540 (2014).
[10] J. J. Keller and Y. P. Chyou, "On the hydraulic lock exchange problem," J. Appl. Math. Phys. **42**, 874–909 (1991).
[11] H. P. Gröbelbauer, T. K. Fannelop, and R. E. Britter, "The propagation of intrusion fronts of high density ratios," J. Fluid Mech. **250**, 669–687 (1993).
[12] R. J. Lowe, J. W. Rottman, and P. F. Linden, "The non-Boussinesq lock-exchange problem. Part 1. Theory and experiments," J. Fluid Mech. **537**, 101–124 (2005).
[13] M. R. Jacobson and F. Y. Testik, "On the concentration structure of high-concentration constant-volume fluid mud gravity currents," Phys. Fluids **25**, 016602 (2013).
[14] V. K. Birman, J. E. Martin, and E. Meiburg, "The non-Boussinesq lock-exchange problem. Part 2. High-resolution simulations," J. Fluid Mech. **537**, 125–144 (2005).
[15] J. Étienne, E. J. Hopfinger, and P. Saramito, "Numerical simulations of high density ratio lock-exchange flows," Phys. Fluids **17**, 036601 (2005).
[16] T. Bonometti, S. Balachandar, and J. Magnaudet, "Wall effects in non-Boussinesq density currents," J. Fluid Mech. **616**, 445–475 (2008).
[17] T. Bonometti, M. Ungarish, and S. Balachandar, "A numerical investigation of high-Reynolds-number constant-volume non-Boussinesq density currents in deep ambient," J. Fluid Mech. **673**, 574–602 (2011).
[18] V. K. Birman, B. A. Battandier, E. Meiburg, and P. F. Linden, "Lock-exchange flows in sloping channels," J. Fluid Mech. **577**, 53–77 (2007).
[19] Y. Hallez and J. Magnaudet, "Effects of channel geometry on buoyancy-driven mixing," Phys. Fluids **20**, 053306 (2008).
[20] A. Dai, C. E. Ozdemir, M. I. Cantero, and S. Balachandar, "Gravity currents from instantaneous sources down a slope," J. Hydraul. Eng. **138**, 237–246 (2012).
[21] A. Dai, "Gravity currents propagating on sloping boundaries," J. Hydraul. Eng. **139**, 593–601 (2013).
[22] A. Dai, "High-resolution simulations of downslope gravity currents in the acceleration phase," Phys. Fluids **27**, 076602 (2015).
[23] P. Beghin, E. J. Hopfinger, and R. E. Britter, "Gravitational convection from instantaneous sources on inclined boundaries," J. Fluid Mech. **107**, 407–422 (1981).
[24] T. Maxworthy, "Experiments on gravity currents propagating down slopes. Part 2. The evolution of a fixed volume of fluid released from closed locks into a long, open channel," J. Fluid Mech. **647**, 27–51 (2010).
[25] A. Dai, "Experiments on gravity currents propagating on different bottom slopes," J. Fluid Mech. **731**, 117–141 (2013).
[26] C. S. Jones, C. Cenedese, E. P. Chassignet, P. F. Linden, and B. R. Sutherland, "Gravity current propagation up a valley," J. Fluid Mech. **762**, 417–434 (2014).
[27] L. J. Marleau, M. R. Flynn, and B. R. Sutherland, "Gravity currents propagating up a slope," Phys. Fluids **26**, 046605 (2014).
[28] V. Lombardi, C. Adduce, G. Sciortino, and M. La Rocca, "Gravity currents flowing upslope: Laboratory experiments and shallow-water simulations," Phys. Fluids **27**, 016602 (2015).
[29] J. Allen, *Principles of Physical Sedimentology* (Allen & Unwin, 1985).
[30] T. K. Fannelop, *Fluid Mechanics for Industrial Safety and Environmental Protection* (Elsevier, 1994).
[31] J. Simpson, *Gravity Currents*, 2nd ed. (Cambridge University Press, 1997).
[32] T. Maxworthy and R. I. Nokes, "Experiments on gravity currents propagating down slopes. Part 1. The release of a fixed volume of heavy fluid from an enclosed lock into an open channel," J. Fluid Mech. **584**, 433–453 (2007).
[33] A. N. Ross, P. F. Linden, and S. B. Dalziel, "A study of three-dimensional gravity currents on a uniform slope," J. Fluid Mech. **453**, 239–261 (2002).
[34] R. E. Britter and P. F. Linden, "The motion of the front of a gravity current travelling down an incline," J. Fluid Mech. **99**, 531–543 (1980).
[35] P. G. Baines, "Mixing in flows down gentle slopes into stratified environments," J. Fluid Mech. **443**, 237–270 (2001).
[36] P. G. Baines, "Mixing regimes for the flow of dense fluid down slopes into stratified environments," J. Fluid Mech. **538**, 245–267 (2005).
[37] A. Dai, "Non-Boussinesq gravity currents propagating on different bottom slopes," J. Fluid Mech. **741**, 658–680 (2014).
[38] W. B. Dade, J. R. Lister, and H. E. Huppert, "Fine-sediment deposition from gravity surges on uniform slopes," J. Sediment. Res. A **A64**, 423–432 (1994).
[39] M. Rastello and E. J. Hopfinger, "Sediment-entraining suspension clouds: A model of powder-snow avalanches," J. Fluid Mech. **509**, 181–206 (2004).
[40] G. K. Batchelor, *An Introduction to Fluid Dynamics* (Cambridge University Press, 1967).
[41] T. H. Ellison and J. S. Turner, "Turbulent entrainment in stratified flows," J. Fluid Mech. **6**, 423–448 (1959).
[42] A. Dai, "Thermal theory for non-Boussinesq gravity currents propagating on inclined boundaries," J. Hydraul. Eng. **141**, 06014021 (2015).
[43] C. Härtel, E. Meiburg, and F. Necker, "Analysis and direct numerical simulation of the flow at a gravity-current head. Part 1. Flow topology and front speed for slip and no-slip boundaries," J. Fluid Mech. **418**, 189–212 (2000).
[44] F. Necker, C. Härtel, L. Kleiser, and E. Meiburg, "Mixing and dissipation in particle-driven gravity currents," J. Fluid Mech. **545**, 339–372 (2005).
[45] M. Cantero, J. Lee, S. Balachandar, and M. Garcia, "On the front velocity of gravity currents," J. Fluid Mech. **586**, 1–39 (2007).
[46] T. Bonometti and S. Balachandar, "Effect of Schmidt number on the structure and propagation of density currents," Theor. Comput. Fluid Dyn. **22**, 341–361 (2008).

[47] J. H. Williamson, "Low-storage Runge-Kutta schemes," J. Comput. Phys. **35**, 48–56 (1980).
[48] D. Durran, *Numerical Methods for Wave Equations in Geophysical Fluid Dynamics* (Springer, 1999).
[49] M. Cantero, S. Balachandar, and M. Garcia, "High-resolution simulations of cylindrical density currents," J. Fluid Mech. **590**, 437–469 (2007).
[50] C. Härtel, L. K. M. Michaud, and C. Stein, "A direct numerical simulation approach to the study of intrusion fronts," J. Eng. Math. **32**, 103–120 (1997).
[51] C. Cenedese and C. Adduce, "Mixing in a density driven current flowing down a slope in a rotating fluid," J. Fluid Mech. **604**, 369–388 (2008).
[52] K. B. Winters, P. N. Lombard, J. J. Riley, and E. A. D'Asaro, "Available potential energy and mixing in density-stratified fluids," J. Fluid Mech. **418**, 115–128 (1995).
[53] A. Dai, "On the instability of a buoyancy-driven downflow," Dyn. Atmos. Oceans **71**, 98–107 (2015).